npj | flexible electronics

Article

Published in partnership with Nanjing Tech University

https://doi.org/10.1038/s41528-025-00402-x

Ultra-flexible graphene-metal nanomembrane for wireless applications

Jiejun Zhang[1,2,5], Haitao Jiang[1,2,5], Weida Hong[1,2], Qing Meng[1,2], Zhongying Xue[1], Miao Zhang[1], Paul K. Chu[3], Yongfeng Mei[4], Ziao Tian[1] ✉ & Zengfeng Di[1] ✉

The advancement of wireless communication raises the demand for flexible, high-performance RF antennas for wearable electronics and flexible communication devices. Traditional approaches focused on reducing the thickness of metal films to enhance flexibility which faces limitations due to the skin effect. Herein, a hybrid graphene-Au nanomembrane is produced by one-step delamination processes to address the limitations of traditional metal films, including flexibility and RF functionality. The graphene-Au nanomembrane features a bond-free van der Waals interface, allowing the Au layer move freely with graphene. This structure mitigates the formation of cracks, enhancing the stretchability to over 14% strain and fatigue resistance. Moreover, this composite overcomes the limitations associated with skin depth, consequently enabling an ultra-thin graphene-Au antenna operating at 8.5 GHz for 5 G communications. We also demonstrate wireless image transmission and electromagnetic stealth. The results underscore the significant impact of the innovative design and materials on flexible wireless technology.

The advancement of wireless communication technologies has significantly increased the demand for flexible, high-performance RF antennas used in applications ranging from wearable electronics to flexible communication devices[1–9]. As these applications require materials that can maintain the desirable electrical properties while under various forms of deformation, such as bending, twisting, and stretching, research efforts are primarily focusing on reducing the thickness of metal films to achieve optimal flexibility[10–12]. This approach stems from the understanding that the flexural rigidity of a metal is directly proportional to its thickness[13]. In other words, thinner metal films can be bent more easily, making them suitable for integration into flexible substrates. However, this strategy encounters a critical limitation due to the metal skin depth[14], which refers to the depth at which electromagnetic waves penetrate the metal[15,16]. As the thickness of metal films approaches the skin depth, the conductive layer becomes insufficient to bear the efficient RF signal transmission, thereby degrading the antenna properties. For instance, at a frequency of 2.4 GHz, the skin depths of aluminum, copper, and silver are 1.67, 1.33, and 1.29 μm, respectively[16]. Consequently, most metal-based antennas are thicker than 30 μm[17]. This inherent constraint prevents further reduction of the metal film thickness and poses a significant challenge in the development of ultra-flexible antennas requiring ultra-thin metal films[18].

Graphene has been explored as a potential material for flexible and stretchable electronics due to its high electrical conductivity, excellent mechanical strength, and outstanding flexibility[19,20]. Owing to the dangling-bond-free surface, graphene can be easily combined with other materials, such as metals, polymers, and others, to increase the strength and durability[21]. Moreover, since graphene is capable of reducing the skin effect, it has potential in high-frequency wireless communication[22].

In this work, a hybrid graphene-Au nanomembrane is designed and demonstrated to address the limitations of flexibility and RF functionality plaguing traditional metal films. A wafer-scale graphene-Au nanomembrane with a thickness of 80 nm is prepared by one-step delamination from a germanium (Ge) substrate. A bond-free van der Waals interface at the graphene-Au interface enables the Au nanomembrane to move freely with graphene and prevent the formation of cracks during mechanical deformation, consequently improving the stretchability and fatigue resistance. More importantly, the graphene-Au nanomembrane can be operated below the skin depth of Au, making it ideal for high-frequency wireless communication. As a result, this ultra-thin graphene-Au nanomembrane exhibits ultra-flexibility, enabling arbitrary folding, stretching, and bending, while demonstrating superior mechanical stability with exceptional stretchability (stretching strain >14%) and fatigue resistance (number of cycles > 6×10^4)

[1]State Key Laboratory of Materials for Integrated Circuits, Shanghai Institute of Microsystem and Information Technology, Chinese Academy of Sciences, Shanghai, China. [2]Center of Materials Science and Optoelectronics Engineering, University of Chinese Academy of Sciences, Beijing, China. [3]Department of Physics, Department of Materials Science and Engineering, and Department of Biomedical Engineering, City University of Hong Kong, Kowloon, Hong Kong, China. [4]Department of Materials Science, Fudan University, Shanghai, China. [5]These authors contributed equally: Jiejun Zhang, Haitao Jiang.
✉e-mail: zatian@mail.sim.ac.cn; zfdi@mail.sim.ac.cn

compared to other materials[23–25]. To demonstrate the commercial viability, the ultra-flexible graphene-Au nanomembrane is utilized to fabricate flexible wireless devices, including Wi-Fi antennas and metasurface cloaks. These devices are capable of wireless image transmission and portable electromagnetic stealth, respectively, showcasing the potential of graphene-Au nanomembranes in advanced flexible wireless technology.

Results

Fabrication of ultra-flexible graphene-Au nanomembranes

The fabrication of the graphene-Au nanomembrane is illustrated in Fig. 1a. An 80-nm-thick Au layer is deposited on CVD-grown graphene on a 100 mm Ge substrate by electron-beam evaporation. The Raman spectra of graphene in Supplementary Fig. 1 confirm the high crystalline quality of graphene[26,27]. A semi-rigid-transfer technique is employed to form the crack-free graphene-Au nanomembrane. The process involves peeling the thermal release tape (TRT)-covered graphene-Au nanomembrane with a stiff glass holder and polyvinyl alcohol (PVA) adhesive layer. It also ensures that the Au layer is securely attached to the TRT without delamination. Meanwhile, the Au nanomembrane acts as an adhesive layer, allowing the graphene to be easily delaminated from the Ge substrate[21]. The uniform peeling force exerted by the stiff glass holder prevents structural damage to either the graphene or the gold layer. Afterwards, the glass/PVA/TRT/Au/graphene stack is printed on the flexible substrate. After releasing the glass/PVA/TRT stack, the Au/graphene nanomembrane remaining on the flexible substrate is patterned by photolithography and wet etching to form the top electrode. The optical images of the 100 mm graphene-Au nanomembrane on Ge substrate, Ge substrate after the transfer process, and transferred Au-graphene nanomembrane on the flexible polyimide (PI) substrate are depicted in Supplementary Fig. 2.

Figure 1b shows the photograph of the 100 mm flexible graphene-Au circuit comprising RF antennas, spiral inductors, resistors, and interconnects. Although the graphene-Au nanomembrane is as thin as 80 nm, it has exceptional electrical conductivity and supports operation at higher frequencies (to be discussed later). The graphene-Au nanomembrane offers superior flexibility compared to traditional metal circuits, including the capability to stretch and fold. Figure 1c depicts the photograph of a biaxially stretched graphene-Au circuit, showing remarkably free of structural damage or fissures, confirming the exceptional stretchability and resilience of the graphene-Au nanomembrane. To further illustrate the versatility of the material, Fig. 1d shows the circuit in a state of multiple folds. The circuit on the 100 mm wafer is effectively condensed into a diminutive form of 3×4 cm^2 with a thickness of just 5 mm, that can be conveniently stored in a pocket. The ability to seamlessly transition from an unfolded to a folded state significantly enhances the practical utility of the circuits and renders them well-suited for portable RF electronic applications.

High stretchability of graphene-Au nanomembranes

Figure 2 presents a detailed comparison of the stretchability between Au and graphene-Au nanomembranes, highlighting the impact of incorporating a graphene interlayer. Au nanomembranes tend to propagate cracks linearly when subjected to stretching strains of up to 5%, resulting in the formation of parallel defects that hinder electronic conduction, as shown in Fig. 2a. In contrast, the integration of a graphene interlayer underneath the Au nanomembrane acts as a barrier against crack propagation, effectively preventing the lateral expansion of cracks, as shown in Fig. 2b. To accurately assess the stretchability, experiments are conducted on resistors fabricated with both Au and graphene-Au nanomembranes. The normalized currents at a voltage of 0.1 V are measured under different strains, as shown in Fig. 2c. The insets illustrate the extension of the graphene-Au resistor using a numerically controlled motorized positioning platform. Notably, at a strain of 5%, the resistors constructed from Au nanomembranes exhibit a pronounced decline in the normalized current, indicative of comprehensive crack penetration through the electrodes and significantly reduced conductivity. In contrast, the graphene-Au nanomembrane-based resistors show only slight fluctuations in the normalized current despite strains as high as 14%. This observation suggests a markedly constrained initiation and propagation of cracks in the graphene-Au nanomembranes and underscores the superior mechanical properties and ability to maintain electrical integrity under extensive deformation.

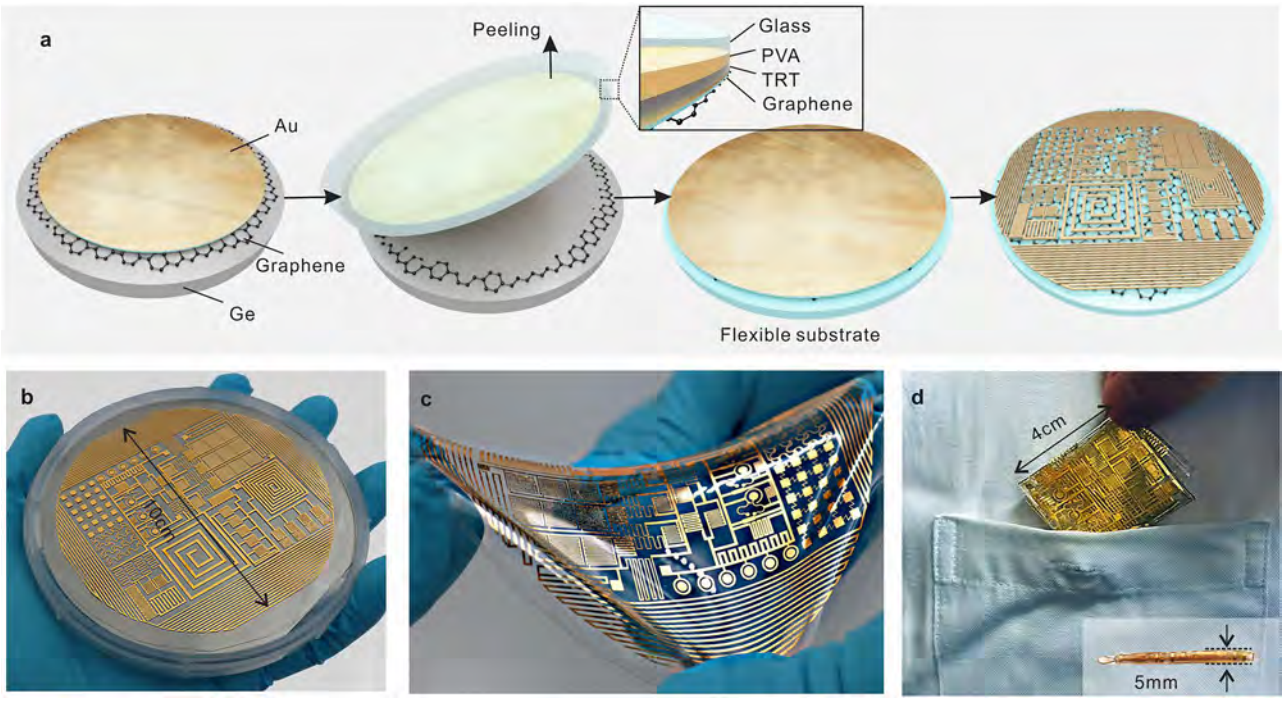

Fig. 1 | Fabrication process and photograph of the 100 mm graphene-Au circuit. **a** Fabrication process of the graphene-Au circuit. **b** Photograph of the 100 mm flexible graphene-Au circuit consisting of RF antennas, square spiral inductors, resistors, and interconnects. **c** Photograph of the biaxially stretched graphene-Au circuit. **d** Photograph of the folded 100 mm circuit, which is tiny enough to fit inside a pocket, with the inset showing the side view of the folded graphene-Au circuit.

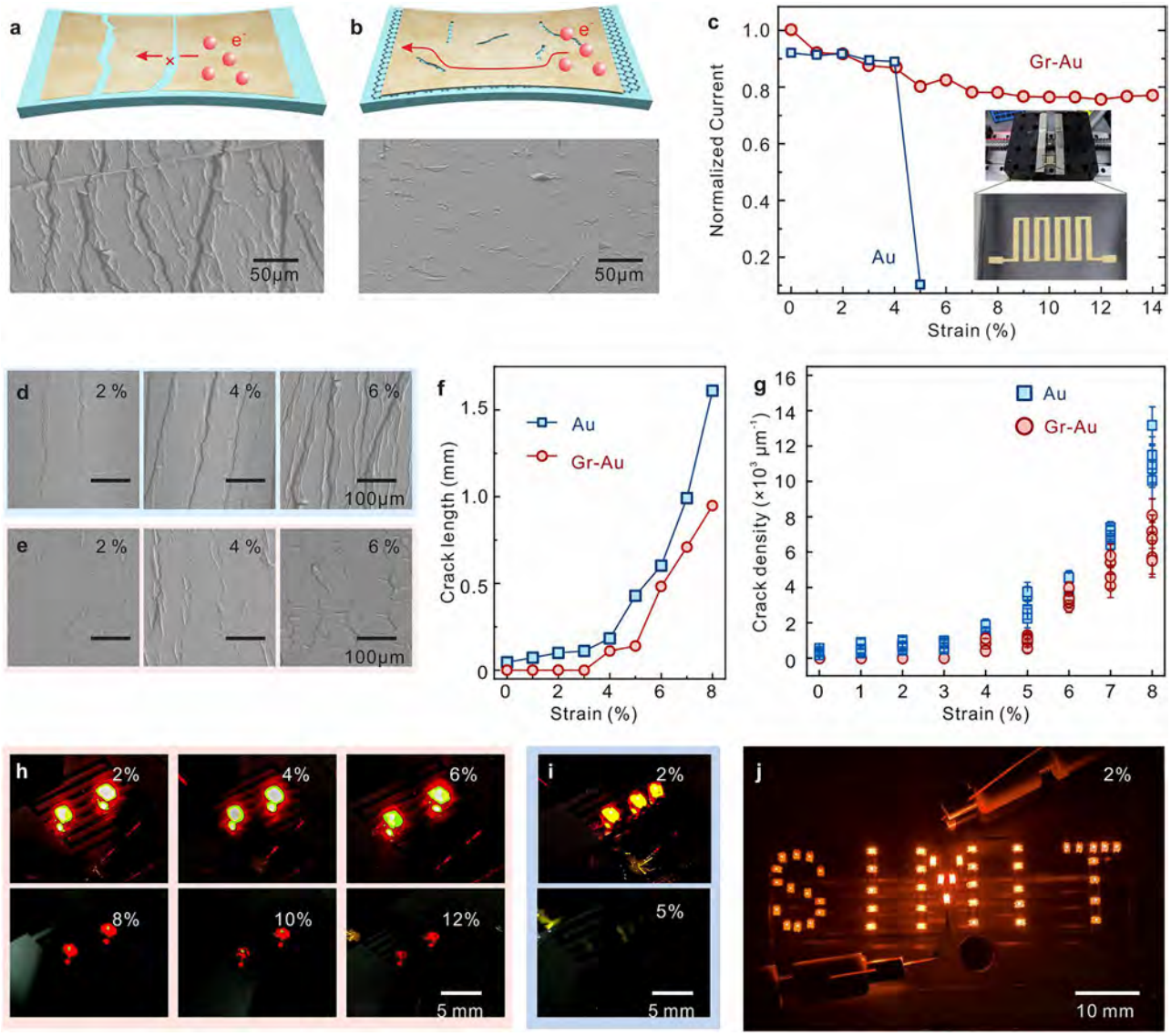

Fig. 2 | Comparative analysis of the stretchability of the Au and graphene-Au nanomembranes. a, **b** Schematic of the fracture behavior (top panel) and corresponding SEM images (bottom panel) of the Au and graphene-Au nanomembranes, respectively. **c** Normalized currents versus strain of the graphene-Au (red line) and Au (blue line) nanomembranes with the insets showing photographs of the graphene-Au resistor being stretched by a numerical control motorized positioning platform. **d**, **e** SEM images showing the morphology of the Au and graphene-Au nanomembranes under varying degrees of strains, respectively. **f** Statistical results of the length of cracks versus strain of the graphene-Au (red line) and Au (blue line) nanomembranes. **g** Statistical results of the density of cracks versus strain of the graphene-Au (red line) and Au (blue line) nanomembranes. **h** Optical images of LEDs powered by 3 V connected to the graphene-Au electrodes under different strains. The LEDs kept luminous when the strain is extended to 12%. **i** Optical images of LEDs powered by 3 V connected to the Au electrodes under different strains for comparison, showing that the LEDs extinguished when the strain exceeds 5%. **j** Optical image of the "SIMIT" logo consisting of 48 LEDs under stretching.

Figure 2d and e illustrate the crack development in the Au and graphene-Au nanomembranes as they are stretched from 2% to 6%. At a strain of just 2%, the Au nanomembranes already exhibit multiple cracks, which tend to widen as the strain increases. In contrast, cracks in the graphene-Au nanomembranes display irregular patterns and deflections, thereby allowing for continued current flow. Supplementary Fig. 3 shows the SEM images on a larger scale. Figure 2f shows the total crack lengths of the Au and graphene-Au nanomembranes, as the strain increases from 0% to 8% (shown by blue and red lines, respectively). This clearly demonstrates that the Au nanomembranes have significantly greater crack lengths than the graphene-Au nanomembranes. Notably, the graphene-Au nanomembranes do not exhibit apparent cracks at strains below 4%. The analysis of the crack density, shown in Fig. 2g, is conducted by optical microscopy in conjunction with the classic OTSU thresholding algorithm (more details can be found in Supplementary Fig. 4 and "Methods")[28,29]. It provides quantitative insights into the structural integrity of these materials under mechanical stress. A higher crack density is observed from the Au nanomembranes compared to graphene-Au nanomembranes under identical strain conditions. The excellent stretchability of the graphene-Au nanomembranes renders them suitable for use as flexible electrodes, as demonstrated in Fig. 2h, which shows LEDs connected by graphene-Au electrodes remain luminous even at a strain of 12%. The luminance of LEDs was influenced by the instable connection from silver glue when strain exceeded 6%. In contrast, LEDs connected by Au electrodes cannot be lit at a strain of 5%, as shown in Fig. 2i. The finding is in alignment with the stretching results in Fig. 2c. The "SIMIT" logo, featuring 48 LEDs interconnected by graphene-Au electrodes (Supplementary Fig. 5), remains brightly lit under a 2% strain, as illustrated in Fig. 2j. The intensity of the LED illumination directly correlates with the applied voltage. The high durability and efficiency of the graphene-Au nanomembranes in maintaining electrical connectivity under strain are demonstrated.

High fatigue resistance of graphene-Au nanomembranes

The emergence of crack initiation sites under continuous loading can produce material failure and shorten the lifespan of applications requiring flexibility[30]. This type of failure is notably more common in metallic materials, where irreversible delamination and stress concentration facilitate the creation of these sites[10,31]. Figure 3a illustrates the progression of cracks in the Au nanomembranes as the number of repeated loading cycles increases. In the Au nanomembranes, delamination is observed under a 3% load for 5×10^3 cycles, leading to the emergence of crack nucleation sites (as shown in the middle panel of Fig. 3a) due to stress concentration. These sites are prone to further expansion during subsequent loading and unloading cycles, ultimately resulting in large, gaping cracks that interrupt electron flow (bottom panel of Fig. 3a). On the contrary, the graphene-Au nanomembranes in Fig. 3b display a distinctly different behavior. The absence of chemical bonds and the presence of van der Waals interactions between the graphene and Au layers allow the nanomembranes to slide and rotate relative to each other. This mechanism effectively accommodates the local tensile or compressive stresses without causing delamination. The inherent reversibility of this sliding action significantly mitigates the stress concentration and forestalls the formation of nucleation sites for cracks. Consequently, even though capillary cracks may form, they do not propagate through the nanomembranes, thereby averting catastrophic failures. The surface morphology of the Au and graphene-Au nanomembranes after 10,000 cyclic loads is shown in Supplementary Fig. 6.

The fatigue properties of Au and graphene-Au nanomembranes are evaluated. As shown in Fig. 3c, the normalized current of the Au nanomembranes decreases to 0.4 after 6000 cycles under a 3% stretching strain, indicative of crack development. After about 10,000 cycles, there is a sharp decline in the normalized current to zero representing extensive crack formation that interrupts the flow of current. In contrast, the graphene-Au nanomembranes (Fig. 3d) have a significantly longer fatigue life exceeding 12,500 cycles, in addition to superior cyclic stability with minimal current losses. Different fatigue experiments with different strains were conducted which current of resistors was measured every 800 times of stretching. The comparative analysis of the fatigue life of Au and graphene-Au nanomembranes under different strains is presented in Fig. 3e. As the loading strain increases from 1% to 3%, the fatigue life of the Au nanomembranes diminishes abruptly from 27,000 cycles to 10,000 cycles. In contrast, the

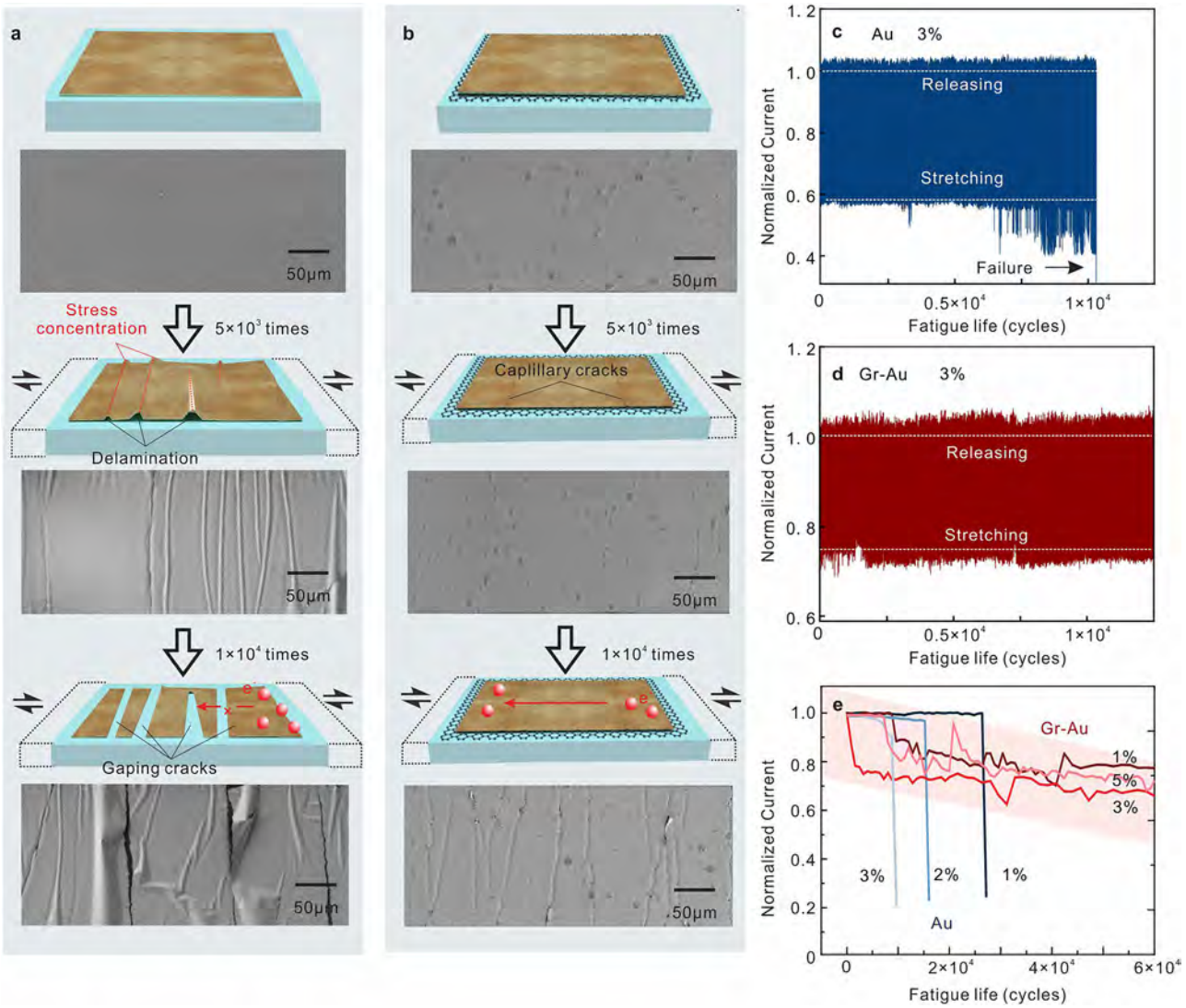

Fig. 3 | Strengthening of the graphene-Au nanomembranes with improved fatigue resistance compared to the Au nanomembranes. a, **b** Schematic of the fatigue behavior of cracks on Au and graphene-Au nanomembranes and corresponding SEM images, respectively. During repeating stretch and recovery, the surface morphology of the Au nanomembranes is always coarser. **c**, **d** Normalized currents of Au and graphene-Au electrodes, respectively, during the fatigue test at a voltage of 0.1 V and 3% strain. **e** Comparison of the fatigue properties of the graphene-Au (red lines) and Au (blue lines) electrodes under different strains at a voltage of 0.1 V.

graphene-Au nanomembranes display remarkable resilience, showing virtually no reduction in the fatigue life even at a 5% loading strain and stability for 60,000 cycles without notable performance degradation. During the loading and unloading cycles, a minor fluctuation in the current is observed due to the random separation and reconnection of capillary cracks. Nonetheless, this fluctuation is minimal and does not adversely affect the overall functionality of flexible applications. The long fatigue life indicates that the graphene-Au electrodes are very durable and stable, making them excellent for flexible applications requiring long-term durability and stability.

Ultra-thin graphene-Au WiFi antenna

In addition to the stretchability and fatigue durability, the RF characteristics of metallic materials play a critical role in flexible wireless applications as they determine the efficiency of RF electronic devices as well as their ability to transmit signals over long distances. There is, however, a limitation imposed by the intrinsic property known as the skin depth, which refers to the thickness of the material where the electrical current responsible for RF radiation flows effectively[15]. For example, the skin depth of Au is 1.59 μm for 2.4 GHz Wi-Fi technology[32]. The thickness required for Au-based antennas is four times larger than the skin depth of Au, as 98% of the current flows through the outer layer[16]. Therefore, antennas should be thicker than 30 μm[17]. This limitation hinders ultra-thin and ultra-flexible wireless applications.

It has been shown that 2D materials can enhance the RF properties of ultrathin metal films by alleviating the skin effect[15]. An optical image of the graphene-Au antenna with a thickness of 80 nm is shown in Fig. 4a. The RF characteristics of this antenna featuring a square spiral configuration are analyzed by the high-frequency simulator software (HFSS), and the results are shown in Supplementary Fig. 7. The working frequency of the graphene-Au antenna is determined by a vector network analyzer (VNA) in the anechoic chamber. The fabrication processes and scattering parameter (S_{11}) of graphene antenna are shown in Supplementary Fig. 8. Figure 4b illustrates

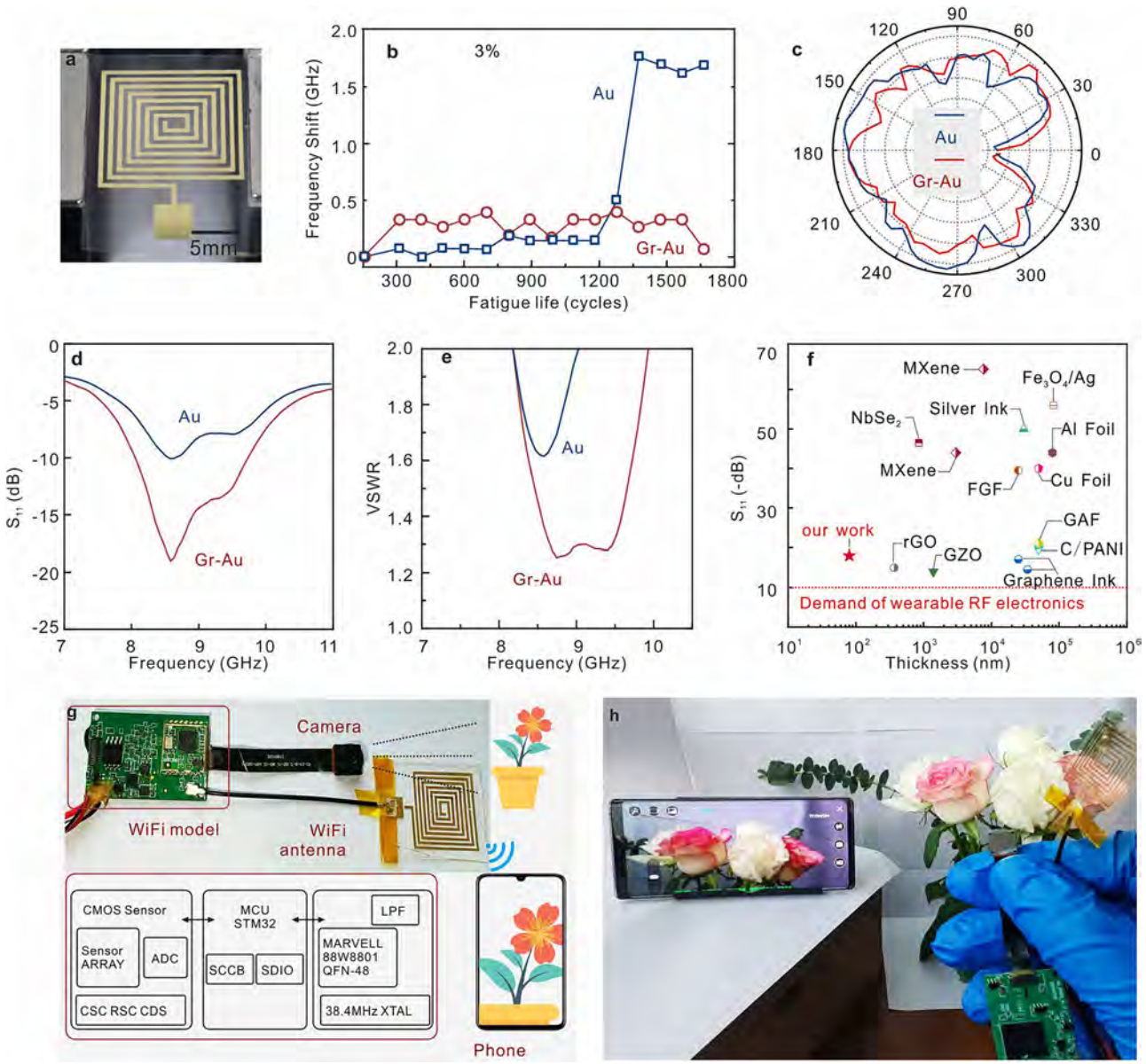

Fig. 4 | Ultra-thin graphene-Au WiFi antenna. a Optical image of the square spiral antenna made of graphene-Au nanomembranes under stretching. **b** Shifts of the resonant frequencies of the antennas made by graphene-Au (red line) and Au (blue line) nanomembranes in the fatigue tests with a strain of 3%. **c**–**e** Two-dimensional radiation patterns, S_{11}, and VSWR spectra of graphene-Au (red lines) and Au (blue lines) square spiral antennas, respectively. **f** Comparison of the S_{11} values with thickness in different studies. **g** Wireless video communication platform consisting of the graphene-Au WiFi antenna, camera, and WiFi module. **h** Clear and precise video output of a mobile phone captured by the camera.

the relationship between the working frequency shifts and fatigue life. At approximately 1350 cycles with a strain of 3%, the operating frequency of the 80-nm-thick Au antenna exhibits a considerable shift of 1.8 GHz. This substantial shift in the operating frequency renders the antenna highly susceptible to environmental changes, leading to potential failure in transmitting and receiving electromagnetic waves at that specific frequency[33]. The changes in inductance and capacitance caused by numerous unrecoverable cracks formed in repeating stretches brought the large shift in resonant frequency. Conversely, the antenna with the graphene-Au nanomembranes has robust stability, with frequency variations confined to a mere 0.3 GHz range. A comparison of the characteristics of the Au and the graphene-Au antennas is shown in Supplementary Fig. 9, demonstrating that the graphene-Au antenna exhibits superior frequency stability under strain and can restore its pristine S_{11} after the release of a 7% tensile strain.

The radiation pattern of the antenna at 8.5 GHz is shown in Fig. 4c. Both the Au and graphene-Au antennas exhibit similar omnidirectional radiation patterns, suggesting that the distribution of RF power radiation is primarily influenced by the physical structure of the antennas. Figure 4d and e compare the S_{11} and voltage standing wave ratio (VSWR) of the Au nanomembranes and graphene-Au nanomembranes with the same thickness of 80 nm. As expected, the Au antennas show limited effectiveness in manipulating electromagnetic waves ($S_{11} = -10$ dB), because the thickness is less than the skin depth of 1.59 μm. Conversely, the graphene-Au antennas with a greater skin depth show improved impedance matching for more effective manipulation of electromagnetic waves, giving rise to a superior S_{11} value ($S_{11} = -20$ dB) compared to Au antennas. As shown in Fig. 4f, the S_{11} values of the graphene-Au antennas and antennas made of other conductive materials with various thicknesses are plotted, and further details are available in Supplementary Table 1. Among the various conductive material-based antennas, the graphene-Au antenna is the thinnest and meets the commercial standards of wearable RF antenna with an S_{11} value greater than 10 dB ($|S_{11}| > 10$ dB).

A wireless video communication platform (Fig. 4g) consisting of the graphene-Au WiFi antenna, camera, and WiFi module is assembled to evaluate the communication characteristics of the graphene-Au antennas. All the tests are performed in real-time using the binary phase shift key (BPSK) modulation. The graphene-Au antenna can transmit information between a mobile phone and a video transfer module operating at 2.4 GHz. The corresponding S_{11} spectrum required at this frequency and radiation pattern are shown in Supplementary Fig. 10. Initially, the camera captures the light signal, which is then relayed to the CMOS sensor and converted into electrical signals. The MCU oversees the entire operation to ensure seamless integration between the digital and analog components. The high-frequency processing segment generates a 38.4 MHz signal through a crystal oscillator, which is subsequently upconverted to 2.4 GHz to serve as the carrier for the encoded video data. Figure 4h and Supplementary Movie 1 show a clear and precise video output on a mobile phone captured by the camera successfully.

Portable graphene-Au metasurface cloaks

A lightweight, thin, and portable electromagnetic stealth cloak plays a crucial role in security and military applications[34,35]. Fig. 5a depicts the schematic diagram of the periodic split-ring array-based graphene-Au metasurface cloak designed to operate at 20 GHz[36]. The geometric parameters of the split-ring unit cell are shown in the inset. During radar detection, electromagnetic waves emitted by and reflected from targets are absorbed by the metasurface periodic structure. Consequently, the electromagnetic waves detected become too weak for the radar to confirm the target's presence. The graphene-Au metasurface cloak offers benefits such as lightweight, portability, foldability and superior absorption capabilities, which markedly improve stealth performance in various scenarios. To mitigate potential disruptions from environmental electromagnetic waves, the setup for measuring radiation patterns is established in a microwave anechoic chamber, as illustrated in Fig. 5b. The inset image demonstrates a metal ball covered by the graphene-Au cloak and effective shielding from detecting electromagnetic waves. Two standard horn antennas operating at 20 GHz are used as a transmitter and detector, respectively. An RF signal generator generates the electromagnetic waves, while a spectrum analyzer measures the incident electromagnetic waves on the detector. Figure 5c displays the radiation patterns of the detector antennas under three different conditions: without metasurface cloaks (yellow line), with Au metasurface cloaks (blue line), and with graphene-Au metasurface cloaks (red line). The radiation patterns observed by the metasurface cloaks show a uniform reduction in detection from all directions, indicating the cloak's effectiveness in diminishing the electromagnetic wave detectability comprehensively[37]. Moreover, the graphene-Au metasurface cloak demonstrates superior absorption compared to the cloak made solely of Au, due to the stronger anti-parallel currents produced by the incident electromagnetic waves in the graphene-Au structure. Supplementary Fig. 11 shows the various shapes of the metasurface units crafted from the graphene-Au nanomembranes, together with the absorption rates at different frequencies. Each shape showcases improved absorption to highlight the large potential of the graphene-Au metasurface cloak in a variety of portable electromagnetic stealth applications[38].

Discussion

Graphene-Au nanomembranes with high stretchability and fatigue durability are designed and fabricated. The bond-free van der Waals interface allows the Au nanomembrane to move freely on graphene to mitigate cracks from developing during mechanical deformation resulting in enhancing stretchability and fatigue resistance. Consequently, the graphene-Au nanomembrane achieves a stretching strain greater than 14% and fatigue resistance for more than 6×10^4 cycles. Moreover, the graphene-Au antenna is able to operate below the skin depth of Au, yielding a high working frequency of 8.5 GHz. This ultra-flexible graphene-Au nanomembrane is adopted in the fabrication of flexible wireless devices, such as Wi-Fi antennas and metasurface cloaks. These devices are demonstrated to wirelessly transmit videos and offer a potential solution for portable electromagnetic stealth applications.

Methods

Sample preparation

The high-quality, large-scale graphene was grown on the Ge(110) substrate on a CVD system at atmospheric pressure, 916 °C, 1.0 sccm CH_4, 70.0 sccm H_2, and 700.0 sccm Ar for 600 min. An 80 nm-thick Au layer was deposited on graphene/Ge by electron-beam evaporation as an adhesion layer, protection layer, and electrode layer. A layer of TRT was attached to Au tightly and the aqueous PVA-0588 solution (8 wt%) was dripped on TRT to adhere to the glass. A piece of glass was laminated on PVA and PVA was dried under ambient conditions. After the PVA had been dried, the glass/PVA/TRT/Au/Gr stack was lifted off and attached to a flexible substrate. The entire sample was heated to a certain temperature to reverse the adhesion of TRT in order to remove glass/PVA/TRT. Photolithography was used to define the electrode patterns, including the 100 mm circuits, resistors, square spiral antennas, and split-ring metasurface. Finally, excess Au was removed by KI/I_2 and the photoresist was removed by acetone. The samples with the Au nanomembranes were directly prepared on PDMS through hard masks.

Mechanical and electrical tests

A numerical control motorized positioning platform and a vernier caliper were used to apply strain, and a probe station was used to apply voltages and measure the currents in the stretch and fatigue tests. During the stretch test, the vernier caliper was used. The samples were fixed to the two arms of the vernier caliper with double-face adhesive tape. The strain on the samples was controlled by changing the length of the vernier caliper. The Au and graphene-Au nanomembranes were stretched under 1–14% strain with a step of 1% for a while and taken to be observed by SEM to examine the crack morphology. In the electrical test, the currents were measured directly while the resistors were stretched. The commercial SMD LEDs were connected to

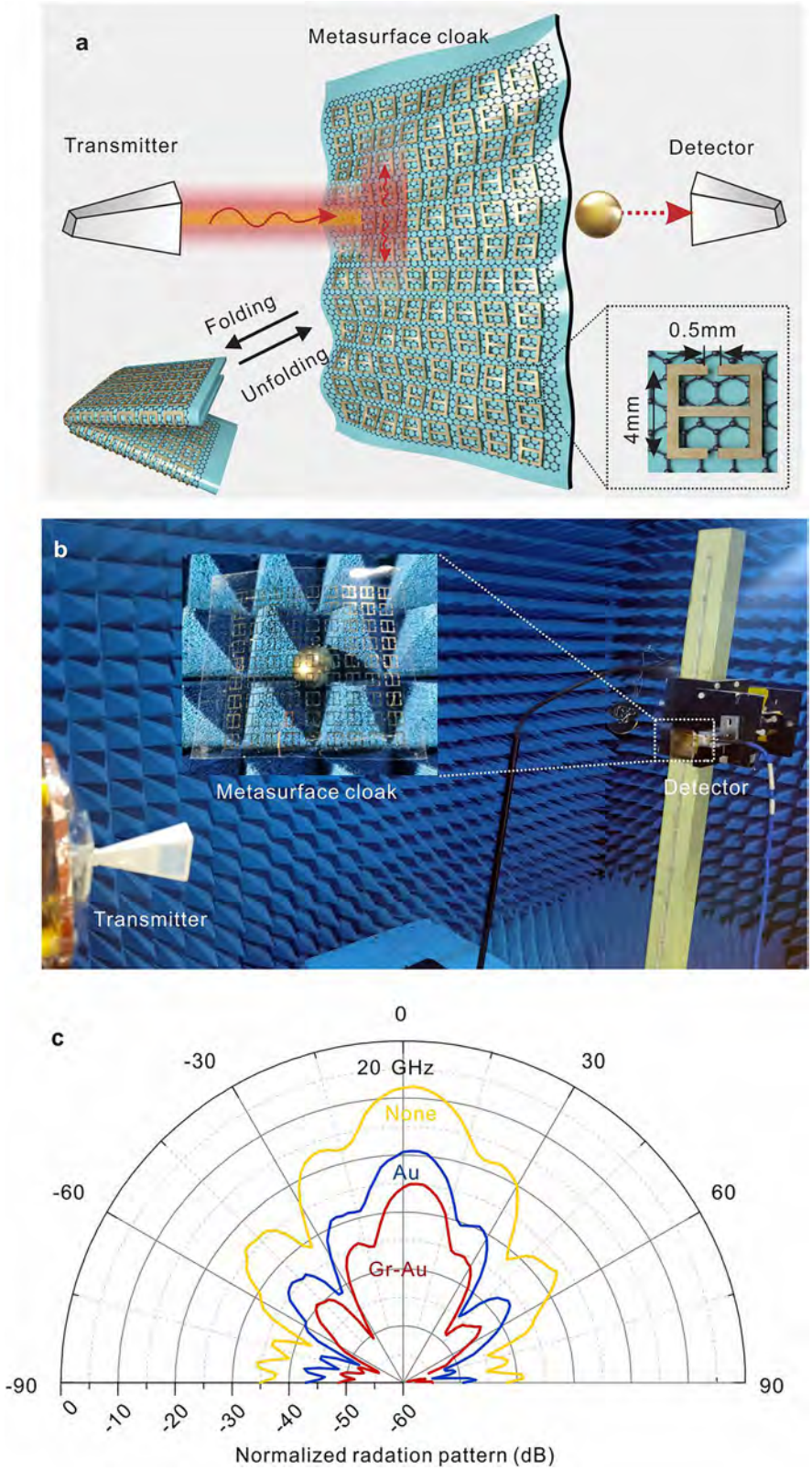

Fig. 5 | Portable graphene-Au metasurface cloaks for electromagnetic stealth applications. **a** Schematic of the graphene-Au nanomembranes used in the metasurface cloak. **b** Evaluation arrangement with the inset showing a metal ball covered by the metasurface cloak. **c** 2D radiation patterns of the antennas under three different conditions: without metasurface cloaks (yellow line), with Au metasurface cloaks (blue line), and with graphene-Au metasurface cloaks (red line).

the electrodes with silver glue. The voltage was applied when a strain was present. During the fatigue test, electrodes and resistors made of the Au and graphene-Au nanomembranes were stretched and recovered for tens of thousands of cycles under the same strain using the numerical control motorized positioning platform and measured after a certain number of cycles.

Observation and image processing of cracks

The Au and graphene-Au nanomembranes were stretched under strains of 0–8% in steps of 1%. After every step, the same areas on the same square samples were observed by optical microscopy. The optical images of the cracks on the samples were converted into grayscale images. The OTSU thresholding algorithm, edge detection

algorithm, and length statistical algorithm were adopted to process the images.

Measurements of antenna and metasurface

The return loss spectra of Au and graphene-Au antennas were evaluated by the vector network analyzer (Keysight PNA-L N5232A) in the frequency range between 300 kHz and 20 GHz. The SMA connectors were directly laminated to the contact electrodes on the antennas and reinforced with silver glue if necessary. To assess the influence of stretching on the return loss, the antennas were measured directly by a vernier caliper under various stretching strains. To evaluate the fatigue strain, the antennas were stretched hundreds of times by a numerically controlled motorized positioning platform under 3% strain. After a certain number of cycles, the antennas were measured and then continued to be stretched. The resonant frequency, the lowest point in the return loss curve, was recorded to determine the frequency shift. The graphene-Au antenna was connected to a commercial video transfer module. The video was transferred to a mobile phone in real-time. To assess the characteristics of the metasurface cloaks, two standard horn antennas operated at 20 GHz, an RF signal generator (Agilent E824C), and a spectrum analyzer (Agilent PXA N9030A) were used in an anechoic chamber. The electromagnetic waves were generated by a signal generator and transmitted by a horn antenna. The frequency spectra for different orientations were acquired by the spectrum analyzer, and the radiation patterns of another horn antenna were acquired automatically. The metasurface cloaks were positioned between two horn antennas, and the radiation patterns were obtained under the same conditions. The radiation patterns of the antennas were also acquired from the same system.

Data availability

The data that support the findings of this study are available from the corresponding author upon reasonable request.

Received: 9 November 2024; Accepted: 19 March 2025;
Published online: 28 March 2025

References

1. Niu, S. M. et al. A wireless body area sensor network based on stretchable passive tags. *Nat. Electron.* **2**, 361–368 (2019).
2. Shen, Q. C. et al. Liquid metal-based soft, hermetic, and wireless-communicable seals for stretchable systems. *Science* **379**, 488–493 (2023).
3. Leng, T. et al. Graphene nanoflakes printed flexible meandered-line dipole antenna on paper substrate for low-cost RFID and sensing applications. *IEEE Antennas Wirel. Propag. Lett.* **15**, 1565–1568 (2016).
4. Xie, Z. Q., Avila, R., Huang, Y. G. & Rogers, J. A. Flexible and stretchable antennas for biointegrated electronics. *Adv. Mater.* **32**, 1902767 (2020).
5. Yamagishi, K., Zhou, W. S., Ching, T., Huang, S. Y. & Hashimoto, M. Ultra-deformable and tissue-adhesive liquid metal antennas with high wireless powering efficiency. *Adv. Mater.* **33**, 2008062 (2021).
6. Zhang, X. et al. Two-dimensional MoS(2)-enabled flexible rectenna for Wi-Fi-band wireless energy harvesting. *Nature* **566**, 368–372 (2019).
7. Liu, Y. R. N. et al. Ultrastretchable and wireless bioelectronics based on all-hydrogel microfluidics. *Adv. Mater.* **31**, 1902783 (2019).
8. Hajiaghajani, A. et al. Textile-integrated metamaterials for near-field multibody area networks. *Nat. Electron.* **4**, 808–817 (2021).
9. Cho, C. et al. Strain-resilient electrical functionality in thin-film metal electrodes using two-dimensional interlayers. *Nat. Electron.* **4**, 126–133 (2021).
10. Lacour, S. P., Chan, D., Wagner, S., Li, T. & Suo, Z. G. Mechanisms of reversible stretchability of thin metal films on elastomeric substrates. *Appl. Phys. Lett.* **88**, 204103 (2006).
11. Lacour, S. P., Wagner, S., Huang, Z. Y. & Suo, Z. Stretchable gold conductors on elastomeric substrates. *Appl. Phys. Lett.* **82**, 2404–2406 (2003).
12. Lu, N. S., Wang, X., Suo, Z. G. & Vlassak, J. Metal films on polymer substrates stretched beyond 50. *Appl. Phys. Lett.* **91**, 221909 (2007).
13. Rogers, J. A., Lagally, M. G. & Nuzzo, R. G. Synthesis, assembly and applications of semiconductor nanomembranes. *Nature* **477**, 45–53 (2011).
14. Mamalis, A., Manolakos, D., Kladas, A. & Koumoutsos, A. J. A. M. R. Electromagnetic forming and powder processing: Trends and developments. *Appl. Mech. Rev.* **57**, 299–324 (2004).
15. Sarycheva, A. et al. 2D titanium carbide (MXene) for wireless communication. *Sci. Adv.* **4**, eaau0920 (2018).
16. Gund, G. S., Jung, M. G., Shin, K. Y. & Park, H. S. Two-dimensional metallic niobium diselenide for sub-micrometer-thin antennas in wireless communication systems. *ACS Nano.* **13**, 14114–14121 (2019).
17. Shin, K. Y., Lee, J. S., Hong, J. Y. & Jang, J. One-step fabrication of a highly conductive and durable copper paste and its flexible dipole tag-antenna application. *Chem. Commun.* **50**, 3093–3096 (2014).
18. Choong, C. L. et al. Highly stretchable resistive pressure sensors using a conductive elastomeric composite on a micropyramid array. *Adv. Mater.* **26**, 3451–3458 (2014).
19. Kim, K. S. et al. Large-scale pattern growth of graphene films for stretchable transparent electrodes. *Nature* **457**, 706–710 (2009).
20. Liu, N. et al. Dominant 100,000-year precipitation cyclicity in a late Miocene lake from northeast Tibet. *Sci. Adv.* **3**, e1700159 (2017).
21. Liu, G. Y. et al. Graphene-assisted metal transfer printing for wafer-scale integration of metal electrodes and two-dimensional materials. *Nat. Electron.* **5**, 275–280 (2022).
22. Kang, J. H. et al. The role of the p38-activated protein kinase signaling pathway-mediated autophagy in cadmium-exposed monogonont rotifer Brachious koreanus. *Nat. Electron.* **1**, 46–56 (2018).
23. Huang, X. et al. Materials and designs for wireless epidermal sensors of hydration and strain. *Adv. Funct. Mater.* **24**, 3846–3854 (2014).
24. Xu, S. et al. Soft microfluidic assemblies of sensors, circuits, and radios for the skin. *Science* **344**, 70–74 (2014).
25. Baumbauer, C. L. et al. Printed, flexible, compact UHF-RFID sensor tags enabled by hybrid electronics. *Sci. Rep.* **10**, 16543 (2020).
26. Ferrari, A. C. Raman spectroscopy of graphene and graphite: disorder, electron–phonon coupling, doping and nonadiabatic effects. *Solid State Commun.* **143**, 47–57 (2007).
27. Ferrari, A. C. et al. Raman spectrum of graphene and graphene layers. *Phys. Rev. Lett.* **97**, 187401 (2006).
28. Hu, H. et al. Elasto-plastic design of ultrathin interlayer for enhancing strain tolerance of flexible electronics. *ACS Nano.* **17**, 3921–3930 (2023).
29. Talab, A. M. A., Huang, Z. C., Xi, F. & Liu, H. M. Detection crack in image using Otsu method and multiple filtering in image processing techniques. *Optik* **127**, 1030–1033 (2016).
30. Stinville, J. C. et al. On the origins of fatigue strength in crystalline metallic materials. *Science* **377**, 1065–1071 (2022).
31. Lee, S. Y. et al. Selective crack suppression during deformation in metal films on polymer substrates using electron beam irradiation. *Nat. Commun.* **10**, 4454 (2019).
32. D. M. Pozar, *Microwave Engineering*, (John Wiley & Sons, 2009).
33. Huang, X. J. et al. Graphene radio frequency and microwave passive components for low cost wearable electronics. *2D Mater* **3**, 025021 (2016).
34. Wang, H. L., Ma, H. F., Chen, M., Sun, S. & Cui, T. J. A reconfigurable multifunctional metasurface for full-space control of electromagnetic waves. *Adv. Funct. Mater.* **31**, 2100275 (2021).
35. Zhang, J., Shao, L. D., Li, Z. F., Zhang, C. B. & Zhu, W. R. Graphene-based optically transparent metasurface capable of dual-polarized modulation for electromagnetic stealth. *ACS Appl. Mater. Interfaces* **14**, 31075–31084 (2022).

36. Tao, H. et al. Metamaterials on paper as a sensing platform. *Adv. Mater.* **23**, 3197–3201 (2011).
37. Yoo, Y. J. et al. Metamaterial absorber for electromagnetic waves in periodic water droplets. *Sci. Rep.* **5**, 14018 (2015).
38. Jayalakshmi, C. G., Inamdar, A., Anand, A. & Kandasubramanian, B. Polymer matrix composites as broadband radar absorbing structures for stealth aircrafts. *J. Appl. Polym. Sci.* **136**, 47241 (2019).

Acknowledgements

The work was supported by the National Key R&D Program of China (Grant Nos. 2022YFB3204800, 2022YFB4400100), National Natural Science Foundation of China (Grant Nos. 51925208, 62122082, 52350209), Science and Technology Commission of Shanghai Municipality (Grant No. 21JC1406100), CAS Project for Young Scientists in Basic Research (Grant No. YSBR-081), Strategic Priority Research Program of the Chinese Academy of Sciences (Grant No. XDB0670000), and City University of Hong Kong Donation Research Grants (Grant nos. DON-RMG 9229021 and 9220061). Some of the experiments were carried out at the Fudan Nano-fabrication Laboratory.

Author contributions

J.Z. and H.J. contributed equally to this work. Z.D. and Z.T. conceived the research. J.Z. and H.J. fabricated the samples and performed the measurements. Q.M. performed the electrical measurements. W.H. contributed to the RF measurements. Y.M., Z.X., and M.Z. contributed to data analysis and discussions. Z.D., Z.T., J.Z., and P.K.C. co-wrote and revised the manuscript. All the authors discussed the results and commented on the manuscript.

Competing interests

The authors declare no competing interests.

Additional information

Supplementary information The online version contains supplementary material available at https://doi.org/10.1038/s41528-025-00402-x.

Correspondence and requests for materials should be addressed to Ziao Tian or Zengfeng Di.

Supplementary Information

Ultra-flexible graphene-metal nanomembrane for wireless applications

Jiejun Zhang[1,2,#], Haitao Jiang[1,2,#], Weida Hong[1,2], Qing Meng[1,2], Zhongying Xue[1], Miao Zhang[1], Paul K. Chu[3], Yongfeng Mei[4], Ziao Tian[1*], Zengfeng Di[1*]

[1] State Key Laboratory of Materials for Integrated Circuits, Shanghai Institute of Microsystem and Information Technology, Chinese Academy of Sciences, Shanghai 200050, China

[2] Center of Materials Science and Optoelectronics Engineering, University of Chinese Academy of Sciences, Beijing 100049, China

[3] Department of Physics, Department of Materials Science and Engineering, and Department of Biomedical Engineering, City University of Hong Kong, Tat Chee Avenue, Kowloon, Hong Kong, China

[4] Department of Materials Science, Fudan University, Shanghai 200438, China

[#] These authors contribute equally

* Corresponding authors: zatian@mail.sim.ac.cn (Z.A. Tian); zfdi@mail.sim.ac.cn (Z.F. Di)

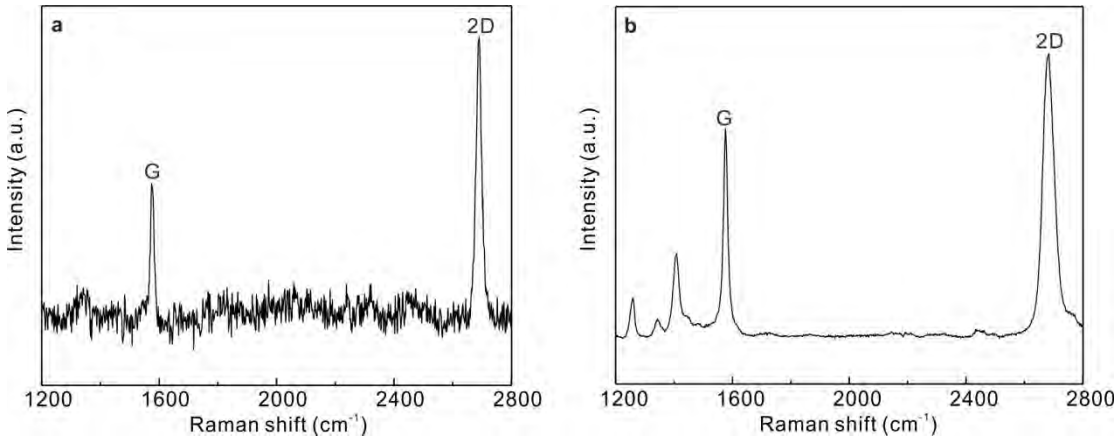

Supplementary Figure 1 Raman spectra of graphene before and after peeling from the Ge substrate. a) Raman spectra of CVD-grown graphene on Ge substrate. b) Raman spectra of graphene on PDMS substrate. The ratio of I_{2D} to I_G is much larger than 1, indicating remarkable graphene quality.

The Raman spectra of CVD-grown graphene on a germanium (Ge) substrate were compared with those of graphene transferred onto a polydimethylsiloxane (PDMS) substrate using one-step delamination process. Raman spectroscopy is a powerful tool for characterizing graphene, with three primary peaks of interest: the G peak (~1582 cm^{-1}), which indicates sp^2 hybridization characteristic of graphene; the 2D peak (~2680 cm^{-1}), which provides information about the number of graphene layers and in-plane strain distribution; and the D peak (~1350 cm^{-1}), which reflects defects in the graphene structure.

As illustrated in Supplementary Figure 1, both the as-grown graphene on Ge and the transferred graphene on PDMS exhibit remarkably similar spectral features. The spectra show minimal D peak intensities, indicating a low defect density in the

graphene samples. Additionally, the high intensity ratio of the 2D peak to the G peak (I_{2D}/I_G) in both cases underscores the exceptional quality of our graphene and the efficacy of our transfer process. These spectral characteristics collectively demonstrate the superior nature of our graphene synthesis and transfer methodology. It is worth noting that the spectrum of graphene on PDMS (Supplementary Figure 1b) displays additional peaks, which can be attributed to the underlying PDMS substrate. These substrate-specific features do not detract from the overall quality assessment of the transferred graphene.

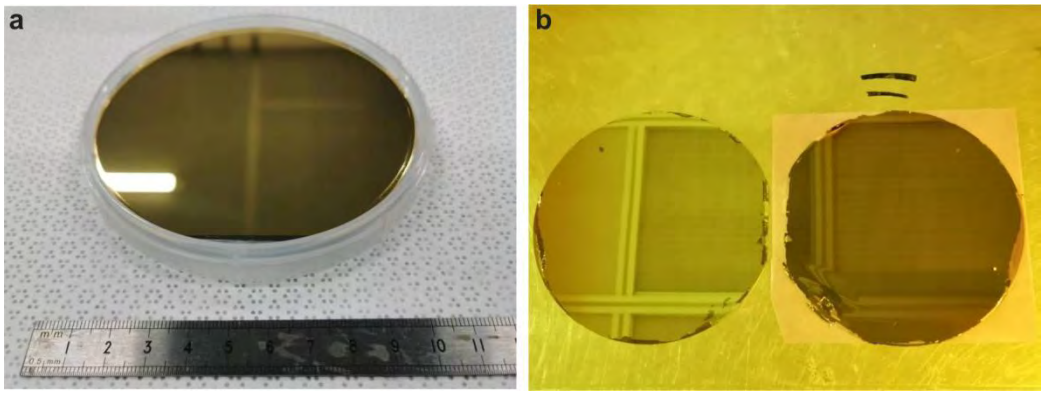

Supplementary Figure 2 Optical images of 100-mm graphene-Au nanomembrane on the Ge and flexible substrates. a) Optical image of 100-mm Au on graphene/Ge substrate. b) Optical image of the Ge wafer after the transfer process (left) and transferred Au/graphene on flexible polyimide (PI) substrate (right).

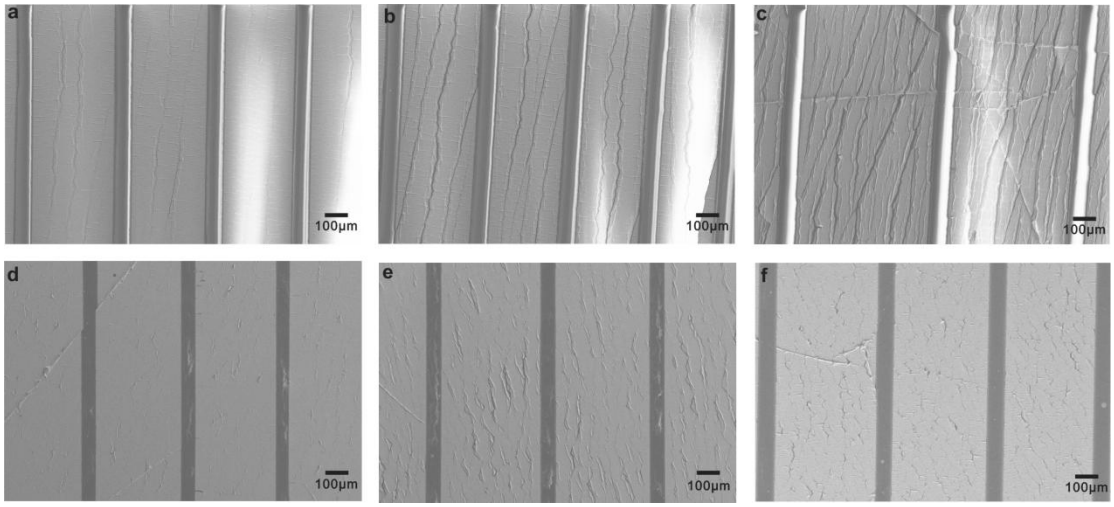

Supplementary Figure 3 Surface morphology of Au and graphene-Au nanomembranes after stretched. a-c) SEM images of Au nanomembranes stretched with 2%, 4%, and 6% strains from left to right, respectively. d-f) SEM images of graphene-Au nanomembranes stretched with 2%, 4%, and 6% strain from left to right, respectively.

Supplementary Figures 3a-c present scanning electron microscope (SEM) images of Au nanomembranes with stripe patterns subjected to uniaxial tensile strains of 2%, 4%, and 6%, respectively, while Supplementary Figures 3d-f display SEM images acquired under identical conditions for graphene-Au nanomembranes. In all cases, the applied strain is oriented along the horizontal direction, resulting in crack formation perpendicular to the strain axis. For Au nanomembranes, distinct cracks are already apparent at 2% strain (Supplementary Figure 3a), with pre-existing cracks widening and new cracks nucleating as strain increases to 4% (Supplementary Figure 3b). At 6% strain (Supplementary Figure 3c), the surface morphology becomes notably

coarse, with numerous straight cracks penetrating the nanomembrane, effectively eliminating conductive pathways. In contrast, graphene-Au nanomembranes exhibit superior mechanical resilience. At 2% strain (Supplementary Figure 3d), the surface remains largely intact with minimal evidence of crack initiation sites. Under 4% strain (Supplementary Figure 3e), only a limited number of small cracks emerge, characterized by their meandering morphology rather than straight trajectories. Notably, at 6% strain (Supplementary Figure 3f), the crack morphology and density remain comparable to those observed at 4% strain, suggesting a plateau in crack propagation. This marked difference between the two cases provides compelling evidence that the incorporation of graphene significantly inhibits both the nucleation and propagation of cracks within the nanomembrane structure.

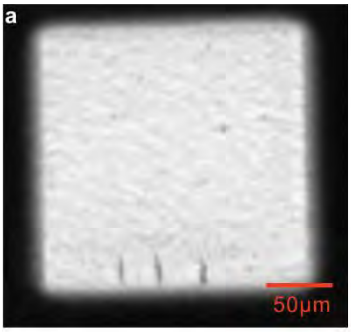

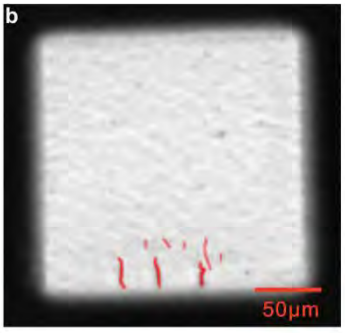

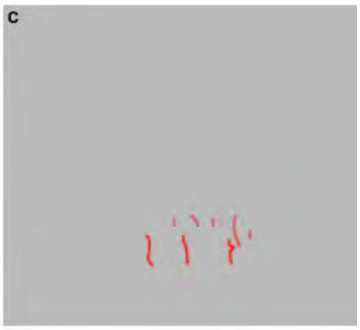

f

crack number	crack length
1	28.9372
2	5.0332
3	25.4243
4	9.5112
5	5.3630
6	20.8081
7	27.8660
8	8.3267

Supplementary Figure 4 Statistical analysis of cracks. a) Optical image of the surface of the Au nanomembranes. The dark lines are the cracks generated with increasing strain. b) Optical image of the surface of the cracks marked by red lines. c) Optical image of extracted cracks with the background eliminated by the algorithm. d) Optical image of cracks processed by the OTSU thresholding algorithm to obtain the binary image. e) Binary image of cracks obtained by the edge detection algorithm. f) Statistical crack amounts and lengths.

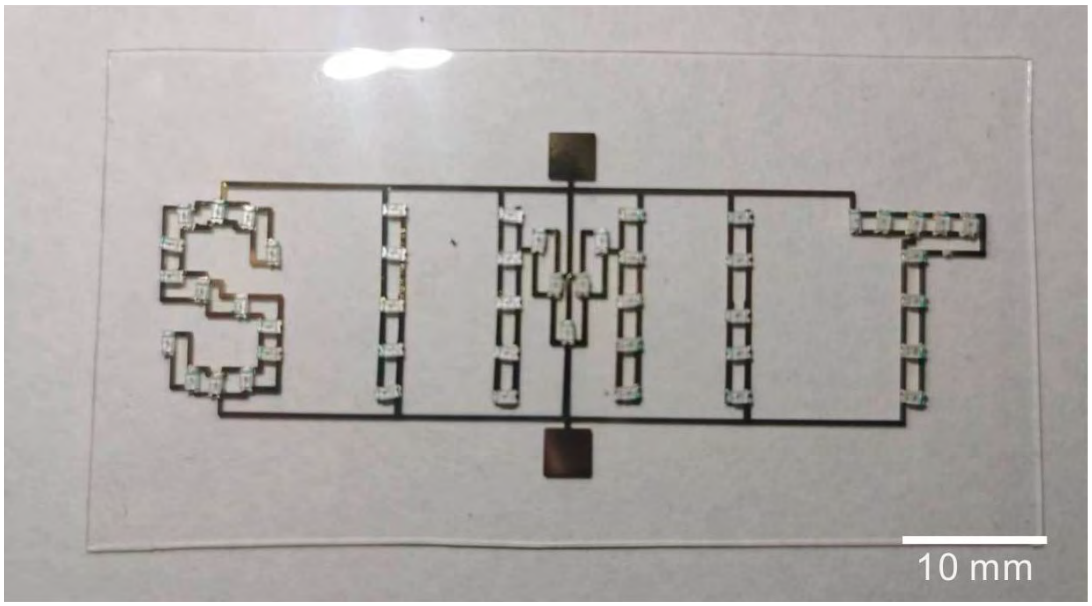

Supplementary Figure 5 Optical image of the “SIMIT” logo comprising 48 LEDs interconnected with graphene-Au electrodes.

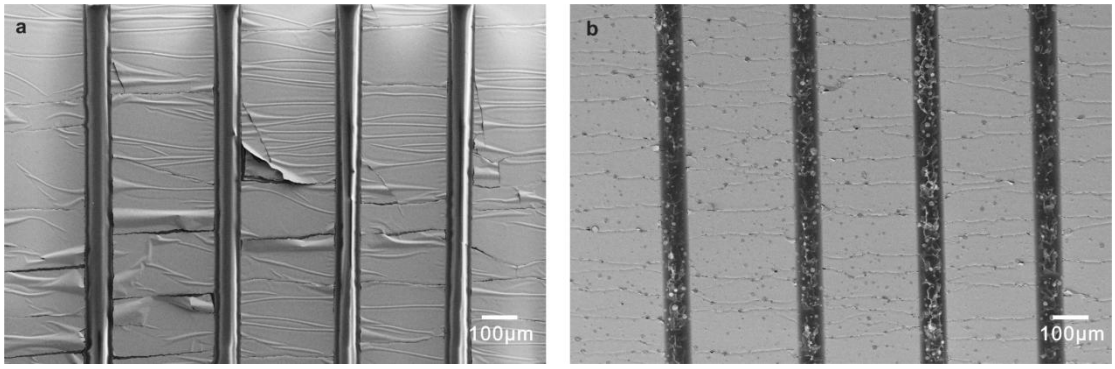

Supplementary Figure 6 Surface morphology of a) Au and b) Graphene-Au nanomembranes after loading for 10,000 cycles under 3% strain from top to bottom.

Au nanomembranes and graphene-Au nanomembranes, both processed to identical patterns, were subjected to fatigue tests using a numerical control motorized positioning platform, with parameters set to a vertical strain of 3% and 10,000 cycles. Scanning electron microscope (SEM) analysis revealed significant differences in structural integrity post-testing. Supplementary Figure 6a depicts Au nanomembranes exhibiting severe degradation, with electrodes separating from the PDMS substrate at numerous locations and cracks propagating horizontally across the entire electrode structure. In stark contrast, Supplementary Figure 6b illustrates the superior performance of graphene-Au nanomembranes, where the surface morphology remains remarkably smooth with no discernible cracks or delamination. These results provide compelling evidence of substantially enhanced fatigue resistance in graphene-Au nanomembranes compared to Au nanomembranes .

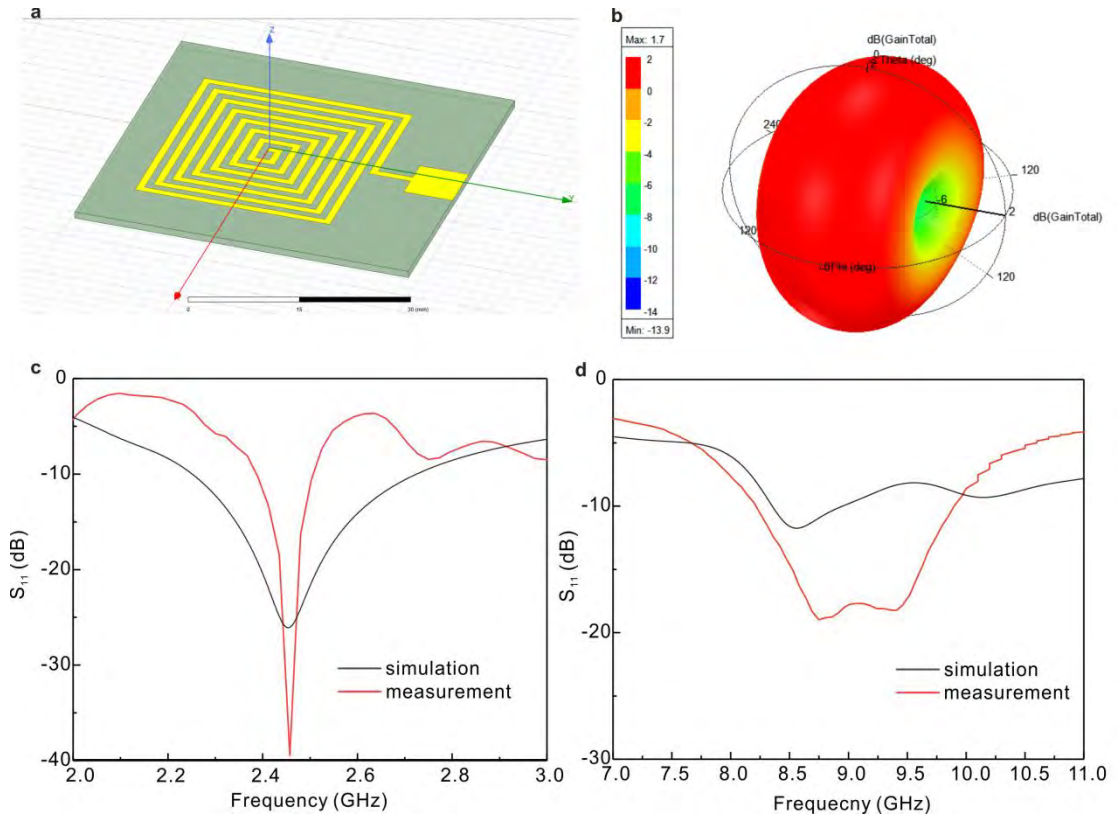

Supplementary Figure 7 HFSS simulation of the square spiral antenna. a) Model of the square spiral antenna. b) Three-dimensional radiation pattern of the square spiral square antenna. Comparison of the spectra of S_{11} between the simulated and experimental results at c) 2.4 GHz and (d) 8.5 GHz.

The performance of the Wi-Fi antenna was simulated using Ansoft High-Frequency Structure Simulator (HFSS), as illustrated in Supplementary Figure 7. Critical parameters, including conductor length, width, and gap width of the graphene-Au antenna, were optimized to ensure operation at 2.4 GHz (for Wi-Fi functionality) and 8.5 GHz (to demonstrate superior flexibility). The final model, depicted in Supplementary Figure 7a, incorporates appropriate material properties for both the conductor and substrate components.

Supplementary Figure 7b presents the simulated 3D radiation pattern of the antenna, exhibiting the characteristic apple shape typical of such designs. The simulated S_{11} curves were compared with measured results across two frequency bands, as shown in Supplementary Figure 7c and d. The resonant frequencies, corresponding to the nadirs of the S_{11} curves, demonstrate close agreement between simulated and measured results in both frequency bands. It is noteworthy that some misalignment exists between the simulated and measured S_{11} curves. This discrepancy can be attributed to two primary factors: the introduction of graphene into the antenna structure and the ultra-thin thickness of the metal layer. These elements introduce complexities that are challenging to model with perfect accuracy in simulation software. Despite these minor discrepancies, the overall correlation between simulated and measured results validates the efficacy of the HFSS simulation in predicting the antenna's performance.

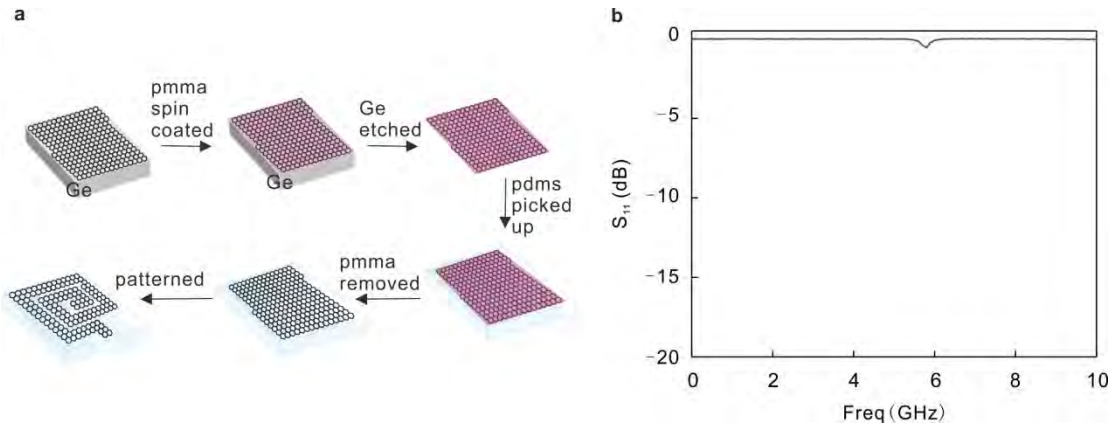

Supplementary Figure 8 Excluding influences causing by graphene in S_{11} tests. a) Fabrication processes of graphene antenna. b) S_{11} spectra of graphene antenna.

As shown in Supplementary Figure 8a, using PMMA as supporting layer, photolithography to define spiral pattern and RIE to remove extra graphene, an antenna based on graphene only was fabricated on PDMS and tested using VNA. As shown in Supplementary Figure 8b, the majority of RF energy was consumed by the resistance of graphene. No obvious signal could be observed which excluded any possible influence from graphene during S_{11} tests.

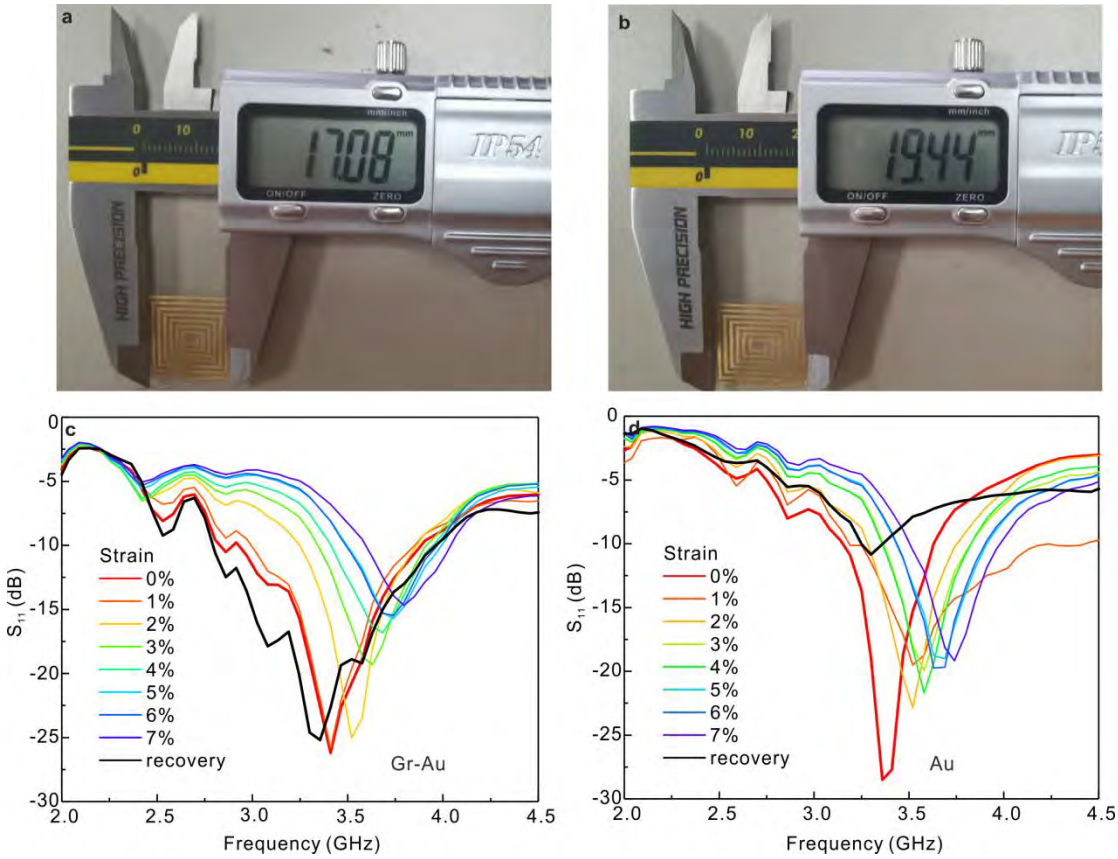

Supplementary Figure 9 Comparison of the stretching performance of two kinds of antennas. a) Optical image of the graphene-Au antenna attached to the Vernier caliper. b) Optical image of the graphene-Au antenna attached to the Vernier caliper under stretching. S_{11} spectra of c) graphene-Au and d) Au antennas under different strains.

Supplementary Figure 9a and b showcase Graphene-Au and Au antennas, fabricated from two distinct nanomembranes, attached to a vernier caliper using double-sided adhesive tape for precise strain application. The antennas underwent incremental elongation in 1% steps up to 7% strain, followed by complete withdrawal. S_{11} curves, measured by a vector network analyzer during and after stretching, are presented in Supplementary Figure 9c and d. As strain increased, both antenna types exhibited reduced S_{11} curve amplitudes and increased resonant frequencies due to

shape deformation. However, the Graphene-Au antenna demonstrated relatively minor alterations in S_{11} characteristics, while the Au antenna showed dramatic changes. Crucially, upon strain withdrawal (indicated by bold lines), the Graphene-Au antenna's resonant frequency recovered significantly, whereas the Au antenna failed to regain functionality, indicating permanent structural damage. These results highlight the superior mechanical resilience and electrical stability of the Graphene-Au antenna design under strain conditions, suggesting its potential for applications requiring flexible or stretchable electronic components.

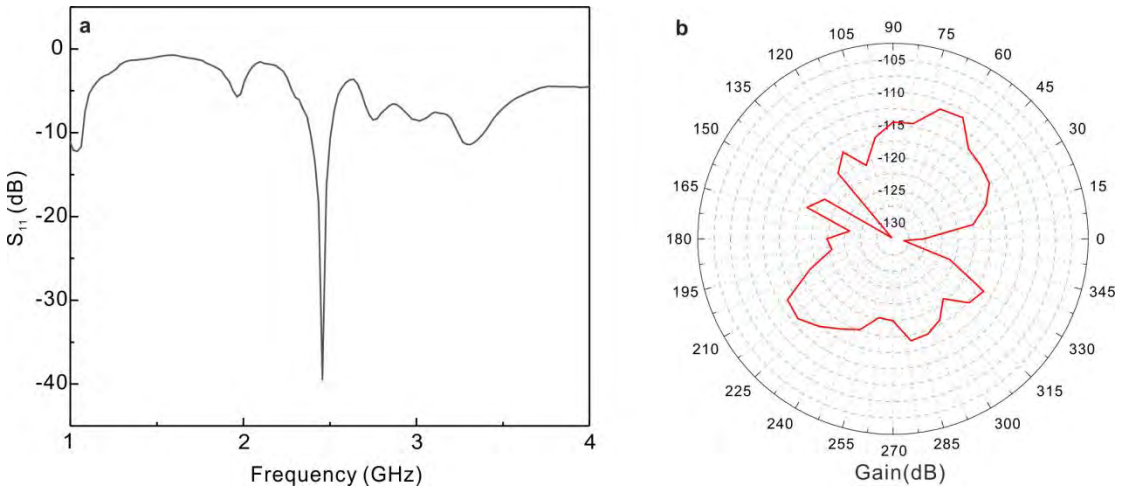

Supplementary Figure 10 Characteristics of the Wi-Fi antenna based on graphene-Au nanomembranes. a) S_{11} spectra of the square spiral antenna around 2.4 GHz and b) Radiation pattern of the square spiral antenna at 2.4 GHz.

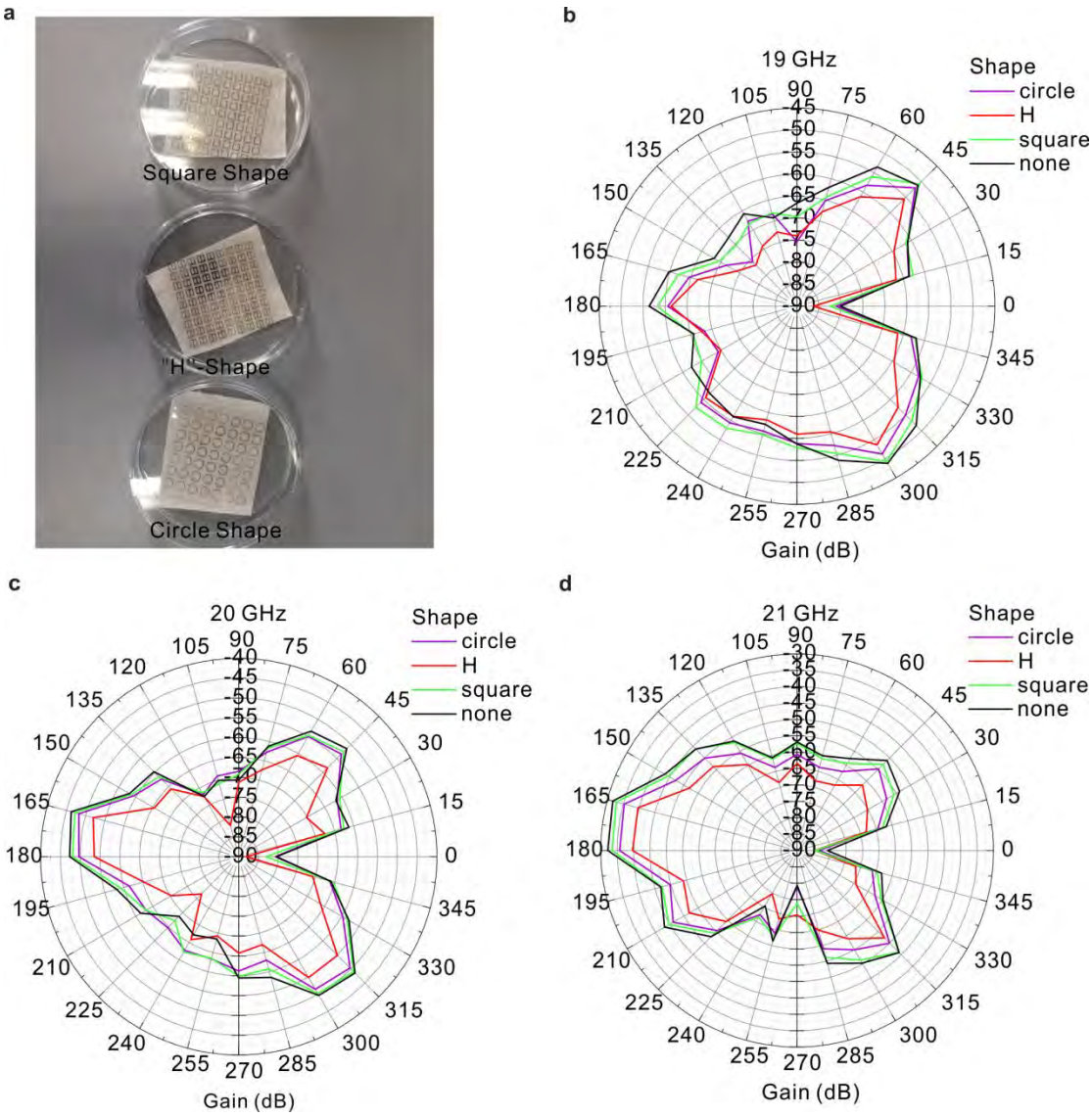

Supplementary Figure 11 Enhanced absorption of the graphene-Au metasurfaces of different shapes at different frequency points. a) Optical image of three kinds of metasurfaces. The metasurface units are square (above), "H"-shape (middle), and circular (bottom). Radiation patterns of different metasurfaces at b) 19 GHz, c) 20 GHz, and d) 21 GHz.

Supplementary Figure 11a presents three types of metasurfaces based on Graphene-Au nanomembranes, featuring unit patterns in circular, square, and "H"

shapes. These metasurfaces were subjected to measurements at various frequency points under identical experimental configurations. Radiation patterns, obtained in an anechoic chamber and illustrated in Supplementary Figures 11b-d, demonstrate the capability of these metasurfaces to attenuate electromagnetic waves. Across most directions, the detected electromagnetic waves were significantly weaker for all metasurface types compared to the control group without metasurfaces. Notably, when evaluated for electromagnetic stealth cloaking applications, the "H"-shaped metasurface consistently exhibited superior performance among the three designs. This comparative analysis highlights the potential of Graphene-Au nanomembrane-based metasurfaces, particularly those with "H"-shaped units, for advanced electromagnetic wave manipulation and stealth technologies.

Supplementary Movie 1 Wireless transfer of vedio captured by camera using graphene-Au antenna.

Supplementary Table 1 Comparison of the characteristics of different antennas.

Materials Systems	**Thickness**	**S_{11} (dB)**	**VSWR**	**References**
Graphene-Au	80 nm	-18.09	1.28	This work
$NbSe_2$	855 nm	-46.50	1.01	Ref. [1]
Graphene Ink	25 um	-17.10	1.32	Ref. [2]
Silver Ink	30 um	-50.00	1.01	Ref. [3]
MXene	3 um	-44.00	1.01	Ref. [4]
MXene	8 um	-65.00	1.00	Ref. [5]
C/PANI	50 um	-19.70	1.23	Ref. [6]
Al Foil	80 um	-44.00	1.01	Ref. [1]
Cu Foil	50 um	-40.00	1.02	Ref. [1]
PVA-Fe_3O_4/Ag	82.6 um	-56.00	1.00	Ref. [7]
GZO	1.4 um	-14.00	1.50	Ref. [8]
AZO	109 nm	-26.00	1.11	Ref. [8]
GAF	50 um	-20.98	1.20	Ref. [9]
rGO	300 um	-15.00	1.43	Ref. [10]
FGF	25 um	-39.53	1.02	Ref. [11]
Graphene Ink	35 um	-13.79	1.51	Ref. [12]

Supplementary References

[1] G. S. Gund, M. G. Jung, K. Y. Shin, H. S. Park, *ACS Nano* **2019**, 13, 14114.

[2] S. Z. Sajal, B. D. Braaten, V. R. Marinov, Ieee, in *IEEE International Symposium on Antennas and Propagation / USNC/URSI National North American Radio Science Meeting*, Ieee, Vancouver, CANADA 2015.

[3] H. Koga, T. Inui, I. Miyamoto, T. Sekiguchi, M. Nogi, K. Suganuma, *RSC Adv.* **2016**, 6, 84363.

[4] W. W. Zhao, H. Ni, C. B. Ding, L. L. Liu, Q. F. Fu, F. F. Lin, F. Tian, P. Yang, S. J. Liu, W. J. He, X. M. Wang, W. Huang, Q. Zhao, *Nat. Commun.* **2023**, 14, 278.

[5] A. Sarycheva, A. Polemi, Y. L. Liu, K. Dandekar, B. Anasori, Y. Gogotsi, *Sci. Adv.* **2018**, 4, eaau0920.

[6] K. Y. Shin, M. Kim, J. S. Lee, J. Jang, presented at *Sci. Rep.*, Sep, **2015**.

[7] R. Carvalho, R. Brito-Pereira, N. Pereira, A. C. Lima, C. Ribeiro, V. Correia, S. Lanceros-Mendez, P. Martins, *ACS Appl. Mater. Interfaces* **2023**, 11234.

[8] J. B. Chemin, N. Adjeroud, V. Kovacova, S. Glinsek, N. Valle, M. El Hachemi, S. Girod, O. Bouton, P. Lunca-Popa, J. P. Maris, *ACS Omega* **2023**, 5475.

[9] R. G. Song, X. Zhao, Z. Wang, H. Q. Fu, K. K. Han, W. Qian, S. Y. Wang, J. Shen, B. Y. Mao, D. P. He, *Adv. Eng. Mater.* **2020**, 22, 2000451.

[10] K. Y. Shin, J. Y. Hong, J. Jang, *Adv. Mater.* **2011**, 23, 2113.

[11] R. G. Song, Q. L. Wang, B. Y. Mao, Z. Wang, D. L. Tang, B. Zhang, J. W. Zhang, C. G. Liu, D. P. He, Z. Wu, S. C. Mu, *Carbon* **2018**, 130, 164.

[12] W. J. Wang, C. Ma, X. T. Zhang, J. J. Shen, N. Hanagata, J. T. Huangfu, M. S. Xu, *Sci. Technol. Adv. Mater.* **2019**, 20, 870.